

PEACHES IV: Tracing the Formation & Evolution of C₂H in Perseus Low-Mass Protostars

JACK G. ANDERSON ¹, JENNIFER B. BERGNER ¹, YAO-LUN YANG ², YICHEN ZHANG ^{3,2} AND NAMI SAKAI ²

¹University of California, Berkeley, Berkeley CA 94720, USA

²RIKEN Cluster for Pioneering Research, 2-1 Hirosawa, Wako-shi, Saitama 351-0198, Japan

³Department of Astronomy, School of Physics and Astronomy, Shanghai Jiao Tong University, 800 Dongchuan Rd., Minhang, Shanghai 200240, China

ABSTRACT

The radical hydrocarbon molecule C₂H is widely detected in various stages of star and planet formation, and has emerged as a useful tracer of high-C/O gas within the photochemically active surface layers of mature (Class II) protoplanetary disks. However, the chemistry and evolution of C₂H within younger (Class 0/I) protostars remains much more poorly understood. Here, using data observed as part of the PEACHES survey along with new ALMA ACA observations, we investigate the C₂H emission towards an unbiased sample of 35 Class 0/I low-mass protostars in Perseus. With this large sample, we identify a clear association between C₂H emission and the protostellar outflow cavity walls, and a consistent spatial anti-correlation between C₂H and SO emission. Together, these trends confirm that C₂H is tracing photochemically active, O-poor gas in these younger sources. We fitted the C₂H spectra with a simple LTE model to yield column density maps, and find values ranging from 10¹⁴ – 10¹⁵ cm⁻² in these sources. We also looked for trends in the C₂H emission morphology as a function of various protostellar evolutionary metrics, but find no clear patterns: the C₂H emission remains spatially extended in most sources, independent of age. This indicates that the transition to the compact C₂H emission observed on the surface of Class II disks must happen rapidly, sometime just after the embedded stage.

1. INTRODUCTION

The process of star formation is kicked off by the gravitational collapse of the densest regions of interstellar molecular clouds. Before they evolve into fully formed star systems, these objects begin the maturation process as protostars. Still embedded in their host molecular cloud, they can be characterized as pre-main sequence stars surrounded by a dense, infalling natal envelope of gas and dust (Lada 1987). In the innermost regions of these objects, material from the envelope accretes onto the newly formed star, setting its final mass and luminosity. On larger scales, this envelope begins to be dissipated by large-scale high-velocity outflows of gas and dust (Arce & Sargent 2006). As these sources evolve, their outer envelope is cleared away, yielding only a host star and mature protoplanetary disk. Between the envelope, inner envelope/proto-disk, and outflows, the protostellar environment is host to a wide range of physical conditions, which can be traced observationally using chemical probes (e.g. Tychoniec et al. 2021).

There is recent evidence that at this point in the formation of the star system, the earliest steps towards planet formation are already taking place (Harsono et al. 2018, Manara et al. 2018, Tobin et al. 2020). This makes protostars the best sites for understanding the physical processes and chemistry governing the initial formation steps of new planetary systems. Because of this connection between the formation of planets and their host stars, understanding the chemical and physical evolution of protostellar environments plays a critical role in our understanding of how planetary compositions are set inside of and beyond our solar system.

Observations of mature Class II disks show a distinctive chemical environment compared to earlier evolutionary stages, characterized by the depletion of key volatiles in the gas and active UV-driven photochemistry (Calahan et al. 2023). The presence of highly-reactive hydrocarbon radicals, namely C₂H, serves as an indicator to this unique chemical environment. Notably, strong C₂H emission has been widely observed towards many well studied disks (Miotello et al. 2019, Bergner et al. 2019), indicating a long-lived hydrocarbon chemical equilibrium (Calahan et al.

2023). Two main factors seem to play a role in driving C_2H formation. Firstly, chemical models and high-resolution ALMA observations show that C_2H can only form efficiently in oxygen-poor, i.e. high C/O, gas (Sakai et al. 2010, Bergin et al. 2016, Krijt et al. 2018, Miotello et al. 2019, Krijt et al. 2020, Bosman et al. 2021, Van Clepper et al. 2022). This is because free gas-phase O will readily lock up gas-phase carbon into the more stable CO. Second, abundant ultraviolet (UV) radiation is required for sustained C_2H production (Bergin et al. 2016, Heays et al. 2017, Bosman et al. 2021, Calahan et al. 2023). This is underscored by the early detections of C_2H in interstellar photodissociation regions (PDRs), which are exposed to high UV fields (Jansen et al. 1995, Nagy et al. 2015). The physical and chemical environments necessary for long-lived C_2H production in the surface layers of mature disks have been well studied, but comprehensive studies of the factors driving C_2H formation in younger, embedded sources are still needed.

C_2H has been detected and mapped in a number of protostellar sources including L1527 (Sakai et al. 2014a, Sakai et al. 2014b), L483 (Oya et al. 2018), IRAS 15398-3359 (Oya et al. 2014, Okoda et al. 2018), NGC 1333 IRAS 4C (Zhang et al. 2018), and CB68 (Imai et al. 2022). In general, the C_2H morphology in these embedded sources is extended. Except for L1527 (Sakai et al. 2017), it appears to trace the low-density cavity regions where the high velocity outflows meet the quiescent envelope in most of the sources (Tychoniec et al. 2021). This is in contrast to the compact C_2H morphology seen on the surface of mature disks. Therefore, at some point there must be a transition from the large-scale outflow morphology seen in young protostars, to the compact disk-associated morphology seen in more mature systems. As of yet, there has not been a systematic survey of protostellar C_2H chemistry which could reveal this transition stage or place constraints on the timescale over which it occurs.

With the aim of obtaining an unbiased view of C_2H chemistry in a large sample of protostars of varied ages, we make use of data available as part of the Perseus ALMA Chemical Survey (PEACHES, Yang et al. 2021) and the MASS Assembly of Stellar Systems and their Evolution with the SMA (MASSES, Stephens et al. 2019) which cover 35 Class 0/I protostars in Perseus. We focus on the C_2H , SO, and CO emission in order to trace the chemistry, morphology and evolution of C_2H in this sample. Our main goals are to (1) disambiguate what C_2H is tracing within the protostellar environment, and whether its formation is driven by then same factors (high C/O, high UV) in embedded sources as is seen in class II disks; and (2) search for evolutionary trends in the C_2H emission morphology, from an extended, outflow cavity structure to a more compact disk-like morphology.

2. METHODS

2.1. Observations

We used ALMA observations of C_2H and SO transitions taken with the 12m array as part of the PEACHES project (Project codes 2016.1.01501.S and 2017.1.01462.S, Yang et al. 2021). All data reprocessing and imaging was performed using CASA (McMullin et al. 2007). The measurement sets were obtained using the ALMA pipeline. Line-free channels were averaged to form continuum measurement sets, on which self-calibration was performed for sources with bright continuum emission to improve signal-to-noise ratio. We performed two to three rounds of manual self-calibration, until minimal gains in SNR were observed. The self-calibration process yielded an average improvement in continuum SNR of 31%, while the major and minor beam axes were changed by an average of 0.2% and 1%, respectively. Line and continuum images were created using the CASA task `tclean`. We produced images for our spatial analysis using Briggs weighting and a robust parameter of 1. Images of 600 by 600 pixels were created, with a pixel size of 0.05". Line images were cleaned to a threshold of twice the rms estimated using line free-channels, using automasking low noise, sidelobe and noise thresholds of 1.5, 3.0 and 3.75, respectively. Moment 0 maps of the lines were then created from the line data cubes by integrating over the velocities of interest. The $N = 7-6$, $J = 6-5$ transition of ground state SO and the $N = 3-2$, $J = \frac{5}{2}-\frac{3}{2}$, $F = 3-2$ C_2H transition were imaged. These transitions were selected for each molecule of interest because of their high signal-to-noise ratio and the overall number of sources in which detections of the transitions were made. See Yang et al. 2021 for a list of all detected molecular transitions. Additional images of S-bearing molecules towards the PEACHES sources can be found in Artur de la Villarmois et al. (2023).

To obtain better flux measurements for column density calculations (Section 3.2), we also used complementary observations taken with the ALMA Atacama Compact Array (ACA; project code 2022.1.00303.S) and combined with the 12m data. The ACA observations, taken in August and September of 2023, target the same PEACHES sources and molecular lines as the original 12m survey. Here only the C_2H spectral window is used, covering the $F = 3-2$,

2–1 and 2–2 hyperfine components of the $N = 3-2$, $J = \frac{5}{2}-\frac{3}{2}$ C₂H transition at ~ 262.06 GHz, with a channel width of 61.035 kHz (~ 0.07 km/s). As before, data reprocessing and imaging was performed using CASA, and line images were created using `tclean`. The 12m and ACA data were imaged together using the ‘mosaic’ gridding parameter, Briggs weighting and a robust value of 2. During imaging, the ACA visibilities were downweighted by a factor of 0.41 to correct for the time-on-source (ToS) ratio between the 12m and ACA observations: from 1:5.8 (actual 89:512 minutes) to an effective ratio of 1:2.4 as recommended by Cortes et al. (2023). Line images were cleaned to a threshold of twice the rms estimated using line free-channels, using automasking low noise, sidelobe and noise thresholds of 1.5, 2.0 and 4.25, respectively. Moment 0 maps of the lines were then created from the line data cubes by integrating over the velocities of interest.

The CO images used in our C₂H spatial analyses come from SMA observations as part of the MASS Assembly of Stellar Systems and their Evolution with the SMA (MASSES) survey (Stephens et al. 2019). The MASSES survey made use of the subcompact, compact and extended configurations of the SMA, covering baseline distances of 9.5–77m, 16–77m and 44–226m, respectively. The 15–1231m baselines of the PEACHES ALMA 12m array data (configuration details provided in Yang et al. 2021), with the addition of the 9–50m baselines provided by the ACA observations, cover similar short-baseline distances. We can therefore directly compare the large-scale emission structures from both the ALMA and SMA observations, and in addition we are able to recover more small-scale detail in the ALMA observations. CO data products were taken directly from the MASSES data release web page through the Harvard data archive (Stephens 2019).

2.2. C₂H Spectral Line Fitting

Maps of C₂H column densities and rotational temperatures were produced by fitting synthetic spectra to the ACA + 12m images at positions where the $F = 3-2$ C₂H emission in the moment-0 maps is above a 3σ threshold. The image cubes were first regridded by a factor of 4, i.e. squares of 2-by-2 pixels were averaged, to increase the signal to noise and sample on spatial scales comparable to the beam. In the spectral line model, we assume that the line profiles of each hyperfine component are Gaussian, that each hyperfine component can be described with the same rotational temperature, T_r , and that the emission is in local thermodynamic equilibrium (LTE). The optical depth at the center of the each hyperfine line i is found via:

$$\tau_{i,0} = \frac{N_T}{Q(T_r)} e^{\frac{E_{u,i}}{T_r}} \frac{g_{u,i} A_{u,i} c^3}{8\pi\nu_i^3} \frac{1}{\sigma\sqrt{2\pi}} (e^{\frac{h\nu_i}{kT_r}} - 1) \quad (1)$$

where N_T the total column density, $Q(T)$ the molecular partition function, and σ is the Gaussian line width. For each hyperfine line, $E_{u,i}$ is the upper state energy, $g_{u,i}$ is the upper-state degeneracy, $A_{u,i}$ is the Einstein coefficient and ν_i is the transition frequency. The total optical depth profile can then be described as:

$$\tau_\nu = \sum_i \tau_{i,0} \exp\left(\frac{-(V - V_i - V_{lsr})^2}{2\sigma^2}\right) \quad (2)$$

where V is the velocity, V_i is the velocity offset of each hyperfine line, and V_{lsr} is the source velocity. Finally, the intensity can be calculated using:

$$I_\nu = [B_\nu(T_r) - B_\nu(T_{bg})] \times (1 - e^{-\tau_\nu}) \times \Omega \quad (3)$$

where B_ν is the Planck function, Ω is the effective angular area of the restoring beam, and T_{bg} the cosmic microwave background (2.73 K).

3. RESULTS

3.1. C₂H and SO Emission Morphology

Previous observations of C₂H in protostars have hinted at a connection between the C₂H emission and the outflow (Oya et al. 2014, Oya et al. 2018, Tychoniec et al. 2021), as well as a possible anti-correlation with SO (Sakai et al. 2014a, Sakai et al. 2014b, Okoda et al. 2018, Artur de la Villarmois et al. 2019). Using the unbiased survey of C₂H provided by the PEACHES dataset, we aim to explore these connections by comparing the C₂H morphology to the outflow tracer CO, as well as SO. In studying these correlations, we are interested in the small-scale emission patterns,

and therefore use the 12m-only images for our analysis. Figure 1 presents an overview of the PEACHES sources and detected molecules of interest. The two sources where continuum emission is not detected, SVS 3 and L1448 IRS2E, are omitted. Integrated intensity (moment-0) maps were constructed for all the sources where C₂H emission was detected, shown contoured in red. Also included in Figure 1 are integrated maps of SO, contoured in orange. Integrated intensity maps of CO are shown as a greyscale colormap, which includes both red- and blueshifted emission.

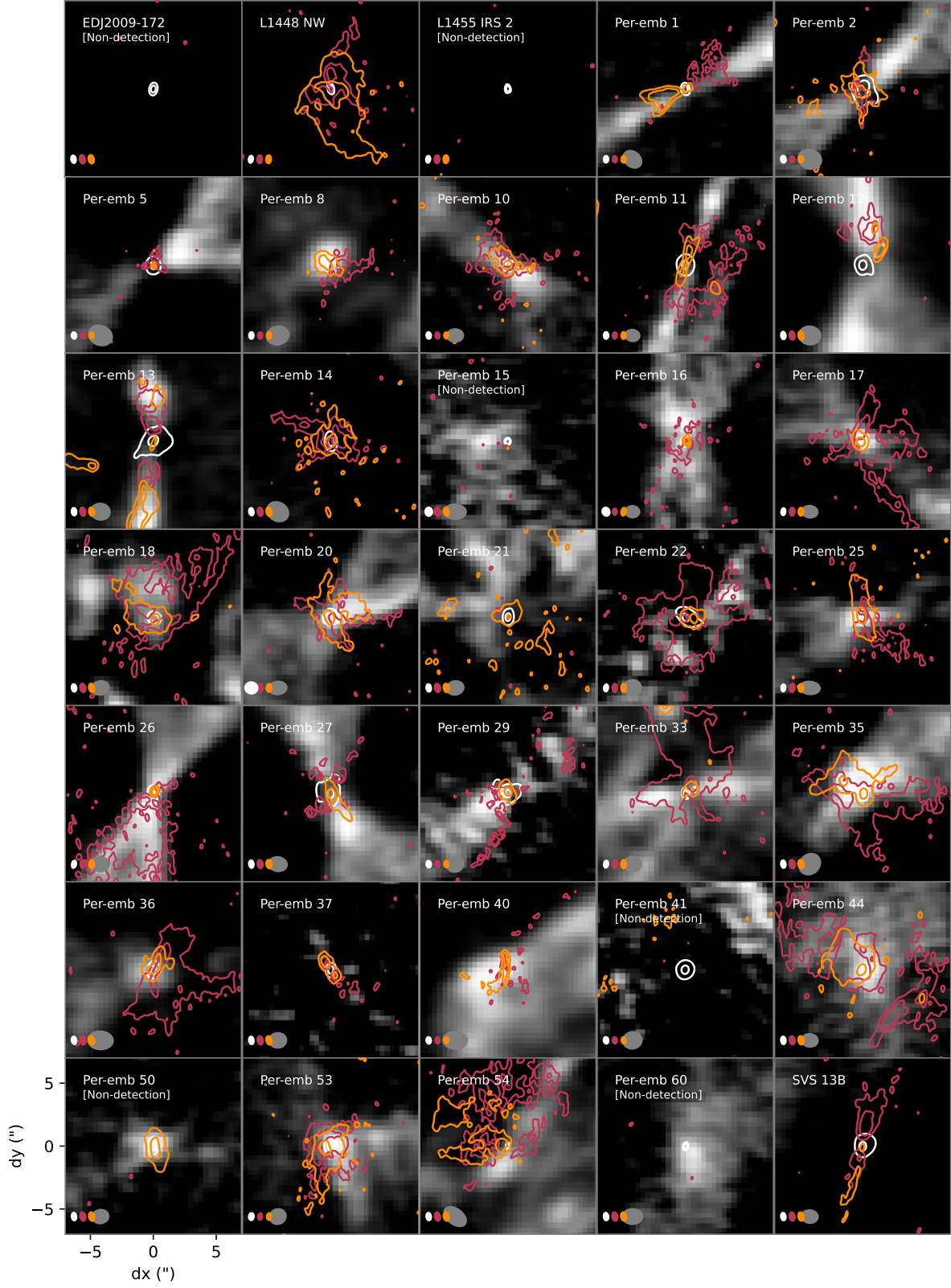


Figure 1. Perseus protostellar sources with continuum detections. Integrated intensity maps of C₂H and SO are contoured in red and orange, respectively. White contours show the mm continuum. Grey colormaps correspond to both the red and blueshifted CO (2-1) emission. Synthesized beams for all maps are provided in the bottom left of each panel.

Of the 35 protostars observed, C_2H and SO were detected towards 30 and 30, respectively. The sources shown in Figure 1 display a wide range of C_2H emission morphologies. Some appear relatively extended (scales of $\sim 3\text{--}4''$) but without discernible structure, (see L1448 NW, Per-emb 18, Per-emb 33, Per-emb 36, Per-emb 44, Per-emb 54). However, many sources exhibit coherent C_2H emission morphologies that suggest a relationship to the outflow structures traced by CO. Several of these exhibit quite narrow C_2H emission (Per-emb 11, 13, SVS 13B), while most others exhibit a X-wing or cone-like emission morphology (Per-emb 1, 2, 5, 10, 14, 17, 20, 22, 25, 26, 27, 29, 35, 53; and to a lesser extent 8 and 12). Interestingly, many of the sources with this cone-like structure are also those where the CO (2-1) moment-0 maps (in greyscale) trace discernible bipolar outflows moving away from the continuum peak. In these cases, we see a clear association between the C_2H emission and the base or edges of the outflow traced by CO.

The SO moment-zero maps (contoured in orange) show a similar range of behavior to that of C_2H , with some directionally extended emission and some more compact emission. However, comparison of SO and C_2H by visual inspection of the moment-zero contours is not sufficient to understand the degree of spatial overlap between the two molecules, especially given that many sources show large azimuthal asymmetries in their emission patterns. To more definitively compare the C_2H and SO emission morphology in the outflowing regions of the protostars, we produce a series of spatial intensity profiles, as shown for an example source in Figure 2. The emission of both molecules of interest is sampled along spatial rays (shown in green) which approximately cover the outflow regions around each protostar. The rays are spaced in 10 degree increments originating at the source continuum peak. The emission from each individual ray is then averaged to give a spatial intensity profile, as shown on the right of Figure 2.

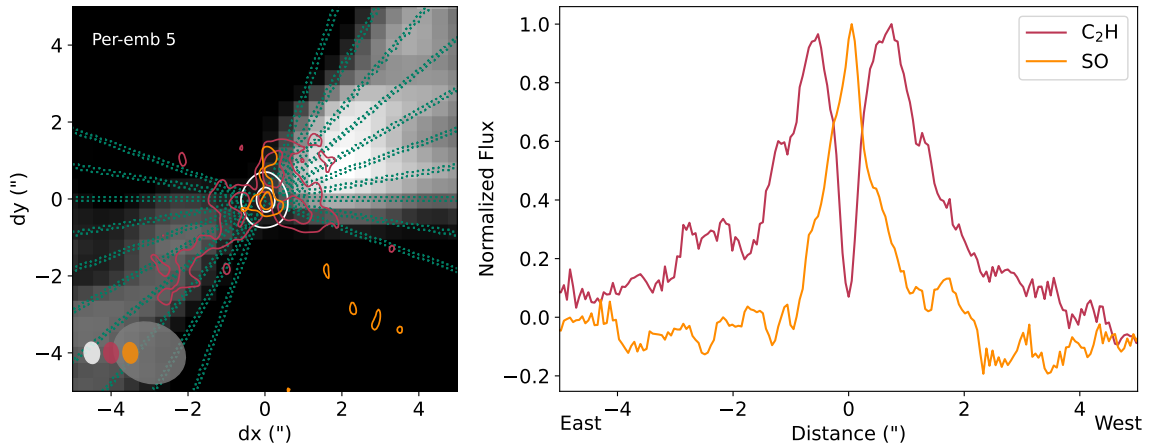


Figure 2. Example spatial analysis of the C_2H and SO emission. Left: red and orange contours correspond to the respective C_2H and SO integrated intensity maps. The grey colormap and white contours in the left image correspond to the CO (2-1) integrated intensity map and mm continuum, respectively. Green lines show the rays along which the C_2H and SO intensity profiles are sampled. Right: spatial intensity profile through the outflow region, made by averaging the profiles along the individual rays. A distance of $0''$ represents the continuum peak.

As shown in Figure 2 for the case of Per-emb 5, this procedure clearly illustrates the difference in spatial morphology between the two molecules. The C_2H is more spatially extended, with emission extending up to $2''$ away from the continuum peak. The SO, as can be visualized in both the moment-zero map and intensity profile, is compact around the location of the continuum maximum, only showing emission within $\sim 1''$ around the continuum peak. What is not clear from the moment-zero contours, but does become evident from the average intensity profiles, is the drop in C_2H emission towards the continuum peak of Per-emb 5, as shown by the dip in the C_2H intensity profile around a distance of $0''$. This coincides with the SO emission peak. Moving away from the continuum peak, the C_2H emission climbs sharply while the SO emission falls off. This type of behavior is very similar to the profile observed in IRAS 15398-3359 (Okoda et al. 2018). To analyze this further, this type of intensity profile analysis was carried out across all sources in the sample where a bipolar outflow could be discerned from the CO (2-1) emission.

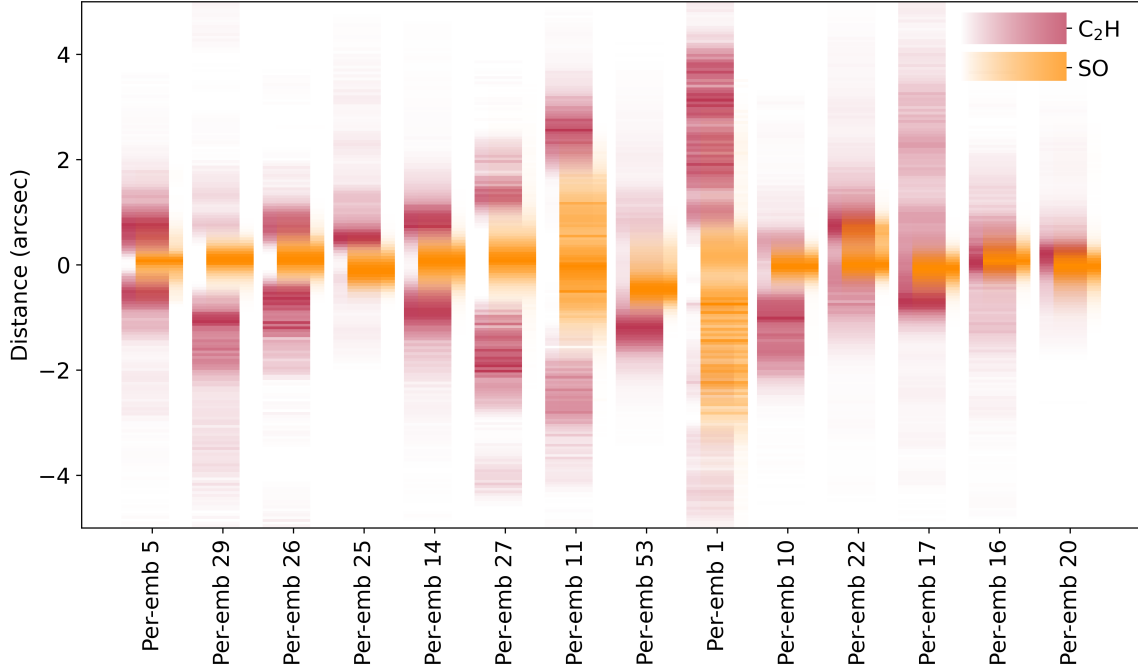


Figure 3. Average intensity profiles of C₂H (red) and SO (orange) for the sources with discernible bipolar outflows. Intensity profiles are sampled only within the outflow region (Figure 2), and distances away from the continuum peak for each source are shown on the y axis. The color transparency represents the normalized flux at each spatial position, with the highest saturation representing the maximum flux across the spatial profile.

Figure 3 shows the resulting intensity profiles in all sources for which this spatial analysis was possible. To enable comparisons across the sources, the average intensity profiles are now plotted with distance as the vertical axis and the relative emission intensity of each molecule shown with color saturation. The sources have been arranged such that similar SO and C₂H morphologies are grouped together. The leftmost sources, Per-emb 5, 29, 26, 25 and 14 all display compact SO around the continuum peak, whereas C₂H is absent from the continuum peak but emits at larger distances beyond the SO peak. Per-emb 10, 22, and 17 also show compact and centrally located SO, with C₂H emission dipping at the SO position but not disappearing entirely. In the center sources (Per-emb 27, 11, 53 and 1), the SO emission is either spatially extended or off-center from the continuum peak; even so the C₂H emission again anti-correlates with the SO emission locations. Per-emb 1 is particularly asymmetric, with strong SO emission within one outflow lobe and strong C₂H emission in the other lobe. This can also be visualized in the moment-zero maps of Per-emb 1 presented in Figure 1. The sources on the right, Per-emb 16 and 20, exhibit compact SO emission, but the C₂H emission does not drop around the the continuum peak and appears more co-spatial with SO. Overall, we find that most sources (12 of 14) show a clear anti-correlation between the location of C₂H and SO within the outflow.

3.2. ACA Images and Column Density Maps

Beyond the characterizing the emission morphology, we also aim to obtain quantitative constraints on the C₂H column densities towards the sources. To do this, we create column density maps using the spectral line model outlined in section 2.2. To ensure complete recovery of the C₂H flux, we use the combined 12m+ACA images for this analysis. To illustrate our approach, the top panel of Figure 4 shows the average spectrum for Per-emb 1 (from all pixels with a $>3\sigma$ detection of the F=3-2 hyperfine component), with the fitted model overlaid in orange. Our C₂H hyperfine transitions span an equal upper state energy, and as a result cannot precisely fit a variable rotational temperature. We proceed with fitting column densities assuming a fixed temperature of 20K, and bound our column density values between 10^{13} and 10^{16} cm⁻², noting that true constraints on the C₂H rotational temperatures, and in turn more precise constraints on the column densities, would require coverage of additional C₂H lines. Our choice of rotational temperature is informed by prior studies of molecular outflows in low-mass protostars, from which rotational

temperatures of 10–50K are typical (Parker et al. 1991, Hatchell et al. 2007, Curtis et al. 2010, Dunham et al. 2010, Dunham et al. 2014a). We adopted a value on the low end of this range under the assumption that the outflow cavities are cooler than the outflowing gas itself. In any case, varying T_r in our spectral line modeling within the 10–50 K range yields changes in calculated C₂H column densities of $< 5\%$.

The maps resulting from fitting all pixels individually are shown in the top panel on the right. Column density maps for all sources with sufficiently bright C₂H emission are shown in the bottom portion of Figure 4. For reference, we also show the CO 2-1 emission (grey colormap) and mm continuum (white contour). All column density colormaps in the lower panel have the same color scaling as the example of Per-emb 1. The fitted column density maps show values spanning $\sim 10^{14} - 10^{15} \text{ cm}^{-2}$, with maps resembling that of the flux, as expected when fitting assuming a fixed rotational temperature. See Table 3 for the median and range of fitted column densities for all sources. The average-per-source uncertainties on our retrieved column densities range from $10^{0.05} - 10^{0.5} \text{ cm}^{-2}$. Most sources show high C₂H column densities close to the continuum max, decreasing moving away from the central star, while some (Per-emb 26, 44, and 54) show peaking C₂H column densities more offset from the continuum max. However, definitive conclusions would require maps of fitted column densities with variable rotational temperatures, only possible with further spectral coverage.

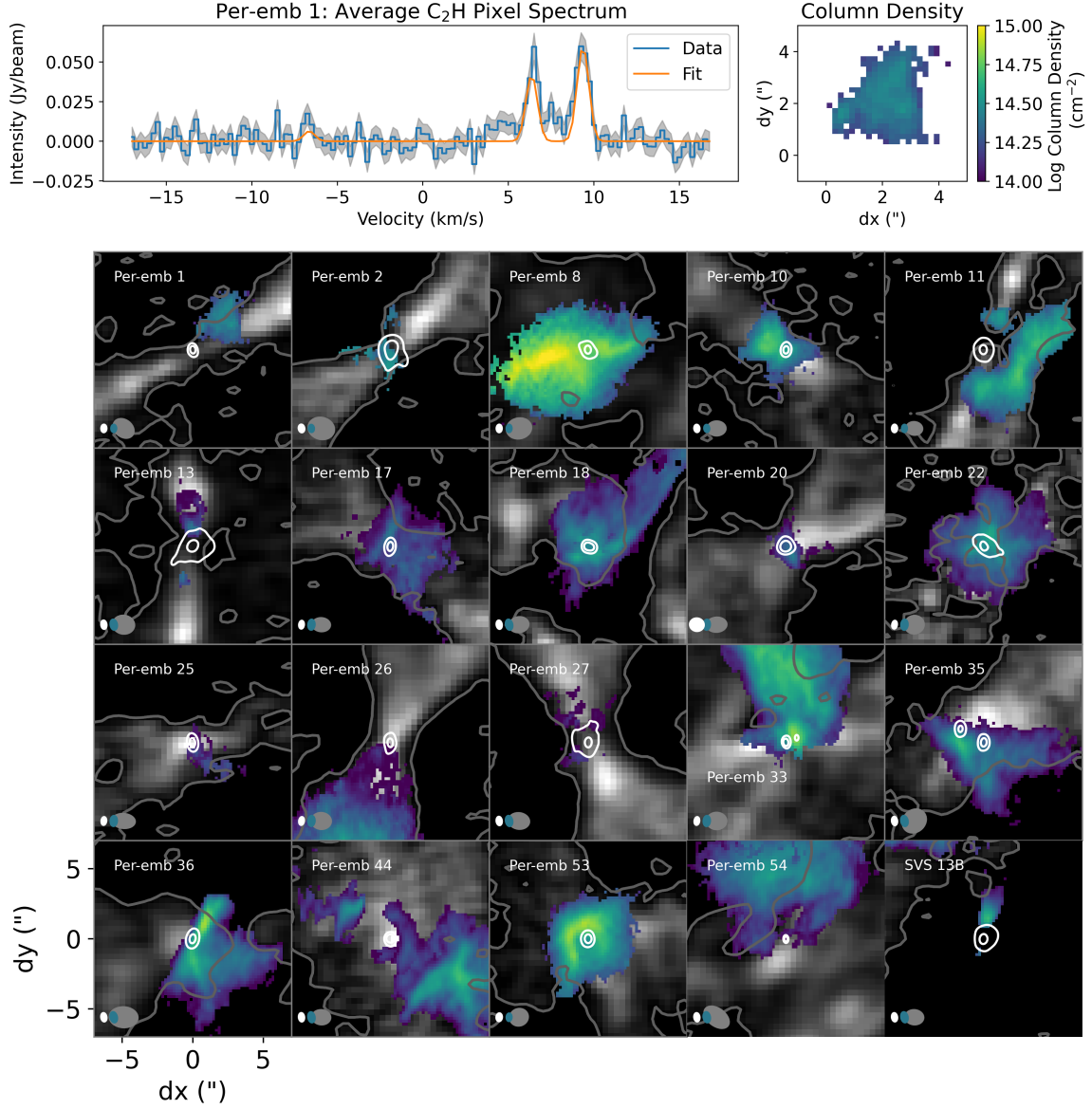


Figure 4. Fitted C₂H column density maps using combined ACA and 12m images. Top row: example spectral line model fitted to the average C₂H spectrum in Per-emb 1 (left, data error plotted in grey), with map of retrieved column density (right). Bottom panel: Fitted column density maps of sources with bright C₂H emission, beam sizes shown in blue. CO (2-1) emission (greyscale colormap with grey contours) and the mm continuum (white contours) are also shown for reference. All column density colormaps have the same color scaling as the example of Per-emb 1.

3.3. C_2H Morphology in Conjunction with Protostar Evolution

Using this large sample of protostellar sources with C_2H detections, we also attempt to identify possible evolutionary trends in the C_2H emission over the course of the protostellar lifetime. In order to do this, we compare the C_2H emission with three evolutionary metrics. As embedded protostars evolve, their central dust disk, best traced in the mm continuum, is expected to increase in size (e.g. Maury et al. 2019). Additionally, their observed luminosities increase and their spectral energy distributions (SEDs) shift towards longer wavelengths (Dunham et al. 2014b). This shift in SED can be described using a blackbody with the same mean frequency, whose temperature increases as the SED shifts towards longer wavelengths. This temperature is defined as the bolometric temperature, and luminosity described as the bolometric luminosity (Myers & Ladd 1993, Myers et al. 1998). We therefore use the mm continuum deconvolved radius, the bolometric temperature and the bolometric luminosity as our evolutionary proxies. In particular, we are interested to see whether the C_2H emission trends from more extended morphologies associated with large-scale outflow cavities to more compact morphologies associated with a (proto-)disk over the duration of the embedded stage.

For this comparison, we estimated the overall spatial extent of the C_2H emission from the width above 3σ of the intensity profiles obtained in Section 3.1. These are plotted in Figure 5 against the three evolutionary metrics. The bolometric temperature and luminosity values and uncertainties are taken from Tobin et al. 2016, while the deconvolved radii are determined via the CASA task `imfit`. The sources clearly vary in spatial extent of the C_2H emission, however there is no clear discernable trend with respect to our evolutionary metrics. The C_2H emission may be either extended or compact for both less mature and more mature systems.

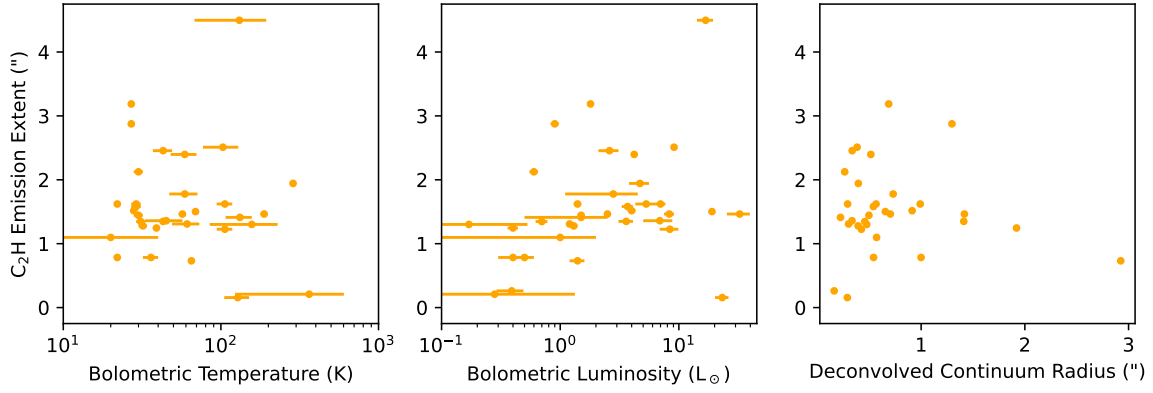


Figure 5. C_2H emission extent as a function of protostellar evolution. The width above 3σ of the C_2H spatial intensity profile is plotted with respect to the three evolutionary metrics: bolometric temperature and luminosity (Tobin et al. 2016; uncertainties shown with errorbars) and mm deconvolved radius. For sources where bipolar outflows could not be identified, the intensity profiles are sampled along all directions from the continuum.

3.4. Kinematic Comparison of C₂H with CO

We also make use of the C₂H fitting procedure outlined in Section 2.2 to extract basic kinematic information from the observations and compare that to the outflows as traced by CO. From our fitted spectra we calculate the shift in the C₂H F=3-2 hyperfine component with respect to the source velocity, and compare that to the intensity-weighted velocities (moment-1) of the CO observations. These maps are shown in Figure 6. Most sources show some red- or blue-shifting of the C₂H emission, though with a fairly small magnitude of ~ 1 km/s, still much larger than the 0.07 km/s velocity resolution of our observations.

In Per-emb 1, 10, 11, 17 and 26, the C₂H emission most closely traces bipolar outflow cavities (Section 3.1). Of these, the C₂H in Per-emb 10 appears very close to the rest velocity. Per-emb 11 and 17 show gradients in the C₂H kinematics that appear correlated with the kinematic structure of CO, with a transition from red-to-blueshifted emission across the two lobes of the outflow. Interestingly, this pattern holds for both of the outflow-like structures near Per-emb 11. In Per-emb 1, 26, and 27, C₂H only traces one outflow lobe, but in both cases shows redshifted emission consistent with the CO kinematics. Per-emb 33 also shows similar kinematic trends between C₂H and CO, but has less clearly defined outflow structure. Note that in all cases, the magnitude of the C₂H red-or blue-shifting is much lower than the CO velocities. Still, these correlations suggest some connection in the velocity structure between the gas of the outflow cavity and that of the outflow itself. In several sources where no bipolar outflow is clearly identifiable, the C₂H emission is uniformly blueshifted (Per-emb 22, 35, 36, 53), possibly due to the extinction of emission originating on the far side of the protostar.

It is important to consider whether radiative transfer effects may be influencing our comparison between the CO and C₂H kinematics. We appear to be tracing optically thinner, higher-velocity CO from the inner region of the outflows, rather than optically thick CO which would originate from the outflow's outer layers at a lower velocity shift. Therefore, we do not expect that optical depth effects are responsible for any differences in red/blueshift between the two species.

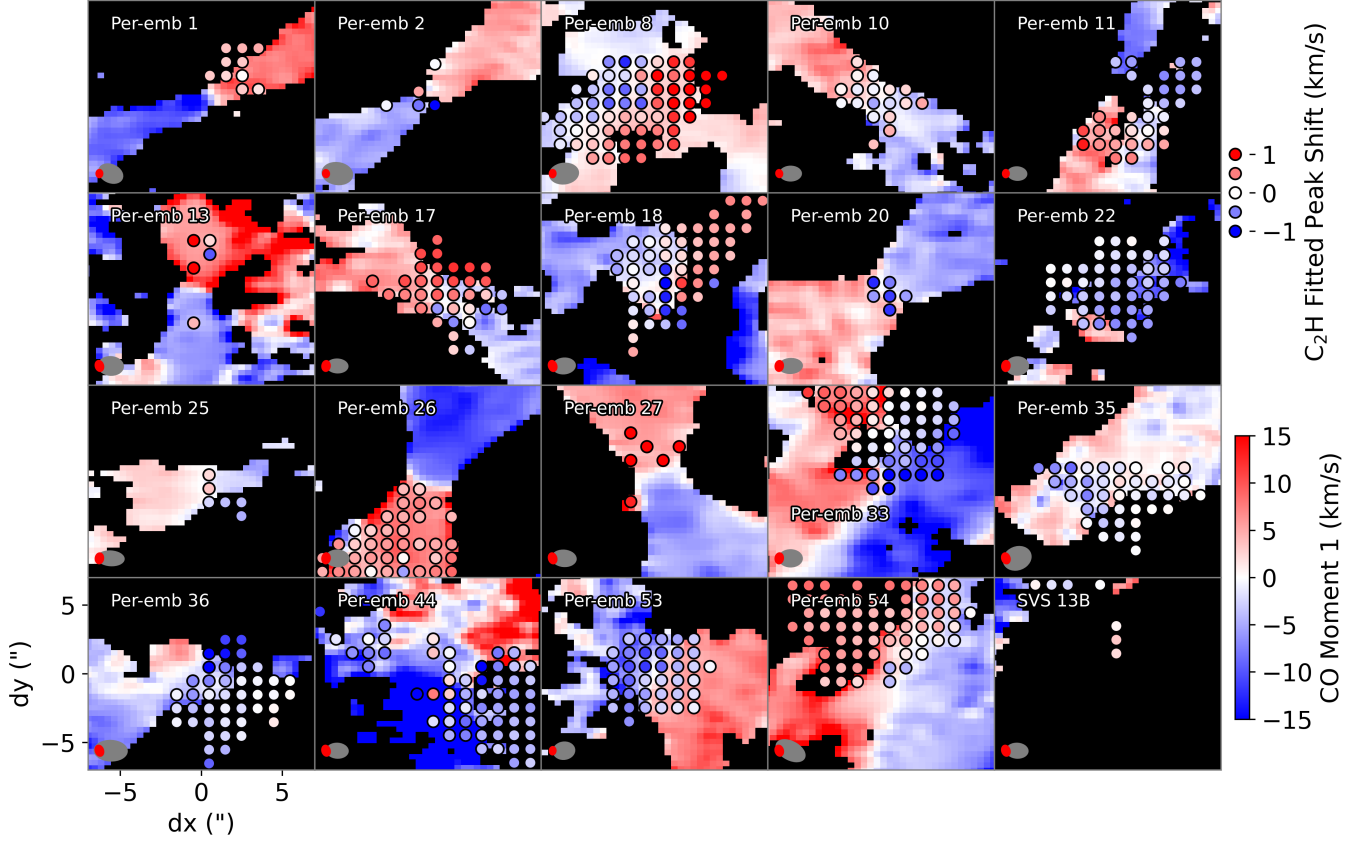


Figure 6. Kinematic comparisons between C₂H and CO. Moment-1 maps of the CO are shown as a colormap, while the coloring of the C₂H circles correspond to the shift in velocity of the fitted F=3-2 hyperfine component, based on the spectral fitting done in section 3.2. The grey and blue ellipses in the bottom corner of each image correspond to beam sizes of the CO and C₂H observations, respectively.

4. DISCUSSION

4.1. *Evolution of C₂H chemistry*

This large sample of low-mass protostars provides an opportunity to search for evolutionary patterns in the emission morphology of C₂H. As protostars begin to clear away their envelope and mature towards Class II systems, the photochemically active regions could be expected to evolve (e.g. Bergner et al. 2020). In particular, at some stage before ~ 1 Myr, photochemistry must become active on small scales at the disk position based on the C₂H morphologies seen in Class II disks (Bergin et al. 2016, Bergner et al. 2019, Guzmán et al. 2021). Figure 5 shows, however, that there is no clear correlation between the C₂H emission extent in these Class 0/I sources and the evolutionary metrics of bolometric temperature/luminosity or continuum radius. This can also be seen through visual inspection of Figure 1, in which the sources are ordered in terms of increasing bolometric temperature (or increasing maturity). While there are some systems with more compact C₂H emission confined to the outflow base (Per-emb 2, 5, 10, 16, 20, 27), which could approximately correspond to a proto-disk surface, there is no obvious evolutionary association. One caveat is that we cannot rule out whether there is a compact C₂H component on even smaller spatial scales than we can access with the spatial resolution of these observations.

The fact that the C₂H emission morphology does not apparently evolve during the Class 0/I lifetime implies that a rapid change must happen at the Class I/Class II transition. The detection of bright, compact C₂H emission even in relatively young $\lesssim 1$ Myr Class II disks (Miotello et al. 2019; Bergner et al. 2019) means that small-scale photochemistry must ‘turn on’ soon after the embedded protostar phase. This fast photochemical transition is one of several dramatic chemical changes that seems to occur during the transition from Class I to Class II systems, along with the rapid depletion of CO (Zhang et al. 2020, Bergner et al. 2020) and H₂O (Harsono et al. 2020). Studying the volatile chemistry in intermediary sources between the embedded protostellar and mature disk stages will be crucial to disentangling these processes.

4.2. *C₂H formation chemistry in embedded protostars*

Our study of C₂H in Perseus protostars provides insight into the underlying C₂H chemistry in these embedded environments. In mature systems, C₂H is associated with the ingredients of high-C/O gas, and high UV fields (Bergin et al. 2016). We show here that C₂H can be used to trace both of these conditions in the embedded stage as well.

The zeroth-moment maps in Figure 1 reveal that many of the Perseus protostars exhibit C₂H emission with a motif of x-wing or cone like structure, which widen moving away from the continuum. The coincidence of these directional, cone or wing-like structures with the edges of the CO emission strongly points to a relationship between C₂H and the overall outflow structure. With this large and unbiased sample, we can confirm the trend between C₂H and outflow cavity walls previously identified in individual protostars: B1-c (Tychoniec et al. 2021), CB68 (Imai et al. 2022), and IRAS 15398–3359 (Oya et al. 2014; Okoda et al. 2018). The presence of C₂H and similar hydrocarbons (e.g. c-C₃H₂ in SMM3; Tychoniec et al. 2021) at the intersection between the outflow and the envelope can be attributed to the prevalence of UV photons in these low density regions, which are needed to produce hydrocarbon radicals. The fact that several protostars do not clearly show this association or it appears incomplete may be due to unfavorable viewing geometries (e.g. if the outflow is pointing toward or away from the line of sight), more complicated source structures or the chemical effects discussed below. Indeed, in all cases where we could clearly identify a bipolar CO outflow structure, we see C₂H emission associated with the base and/or edges of at least one side of the outflow cavity.

We can also investigate the role of gas-phase oxygen in suppressing C₂H production by comparing the C₂H and SO emission morphologies. SO is associated with the sputtering of icy material from grains and therefore serves as a signpost of oxygen rich gas (Bachiller & Pérez Gutiérrez 1997, Jiménez-Serra et al. 2005). Figure 3 shows a clear spatial anti-correlation between C₂H and SO, implying that C₂H production cannot be sustained in gas that is oxygen rich. Indeed, of the 14 Perseus sources where C₂H is present and the outflow could be clearly identified, 12 sources exhibit strong avoidance between SO and C₂H. This behavior in sources where the SO is compact and co-spatial with the continuum (Per-emb 5, 29, 26, 25) could be attributed to differing physical or chemical factors close to the protostar. However, this cannot explain the avoidance of the two species in the sources where the SO emission is offset from the continuum (Per-emb 27, 14, 11, 53, 1). The fact that this trend exists for a range of SO and C₂H structures points to the destruction of C₂H in regions traced by SO.

This behavior is consistent with expectations from chemical modeling: in oxygen rich gas, available gas-phase carbon will react with oxygen or O-bearing species, thereby suppressing the formation of hydrocarbons (e.g. [Bergin et al. 1997](#); [Hollenbach et al. 2009](#); [Du et al. 2015](#)). [Bosman et al. 2021](#) has shown this threshold gas phase C/O ratio is dependent of the UV field strength and overall gas density, but for a UV field to gas density ratio (F_{UV}/n_{gas}) of $10^{-7} - 10^{-5} G_0 \text{ cm}^3$, this hydrocarbon production is quenched as the C/O falls below unity. Interestingly, spatial anti-correlations between small hydrocarbons and SO are also seen in the mature Herbig disks HD 169142 and HD 100546 ([Booth et al. 2023, 2024](#)). C_2H can therefore serve as a reliable tracer to distinguish O-rich vs. O-poor gas within protostellar environments. Indeed, while the SO observed in our sources is likely produced at least in part by weak-shock sputtering of grains ([Zhang et al. 2023](#)), we expect O-rich gas to be present on even smaller spatial scales due to the thermal sublimation of icy material, for instance the spatially unresolved detections of O-bearing complex organics reported in [Yang et al. \(2021\)](#). Higher-resolution observations of organics as well as C_2H would provide a more detailed picture of the balance between O- and C-dominated gas on smaller, disk-forming scales in the protostellar environment.

While the C_2H morphologies are quite different between embedded protostars and mature disks, the column densities are relatively consistent. As shown in Figure 4, we retrieve column densities ranging from $10^{14} - 10^{15} \text{ cm}^{-2}$ with an average C_2H column density across all sources of $10^{14.3 \pm 0.2} \text{ cm}^{-2}$. This is comparable to values estimated in the Class II sources in [Guzmán et al. 2021](#), and to the column densities predicted by PDR chemical models ([Nagy et al. 2015](#)). The similar column densities across these varied contexts points to a formation chemistry dependent on a narrow range of physical conditions: i.e., if C_2H is always formed within a thin gas layer characterized by high UV fluxes, then the resulting column density may be similar even in different astrophysical objects. Note, however, that coverage of additional J-level transitions would improve the precision of our column density retrievals.

5. SUMMARY

Using ALMA 12m and SMA data as part of the PEACHES and MASSES projects and new ALMA ACA observations, we analyze the C_2H emission morphology towards 35 embedded protostars in Perseus.

- We present zeroth-moment maps of the C_2H in the the sources, and show many exhibit a emission morphology which traces the protostar outflow cavity.
- Analysis of the C_2H and SO emission morphologies though the use of outflow intensity traces shows strong spatial avoidance between the two molecules, demonstrating the role of gas-phase oxygen in the formation chemistry of C_2H .
- The C_2H emission morphology appears to not be directly related to protostar age though comparisons of C_2H structure with source bolometric temperature and deconvolved continuum radius, however all sources where C_2H is detected exhibit large, extended structure, indicating the transition in C_2H morphology to what is seen in mature disks must happen rapidly.
- The C_2H spectra of combined 12m and ACA images is fit to a spectral line model, and maps of the fitted column density show C_2H column densities of $10^{14} - 10^{15} \text{ cm}^{-2}$.

Through these observations and analysis, we are able to better understand C_2H morphology and the role of oxygen in the formation of C_2H over a large survey of protostellar sources. Additionally, we better understand the rapid transition that these low-mass sources must undergo from the embedded stage to the mature disk stage, as the photochemically active regions that C_2H trace go from extended and surrounding the outflows to on the surface of the disk once the star is clear of its envelope. To further investigate the difference between the C_2H distribution around Class 0/I sources and that in disks around Class II sources, analyzing the correlation between the outflow opening-angle and the distributions of C_2H and outflow-tracing molecules may serve as a useful diagnostic. Additionally, in some sources with high C_2H abundances, other mechanisms beyond C_2H formation in the cavity wall may need to be considered (e.g. Warm Carbon-Chain Chemistry triggered by CH_4 evaporation [Sakai & Yamamoto 2013](#); [Aikawa et al. 2020](#)). Further studies of C_2H in sources just at the end of their embedded protostar stage may yield more information about when in planet formation period C_2H and other photochemically active molecules may be formed in regions undergoing the very first stages of planet formation.

6. ACKNOWLEDGMENTS

The PEACHES project is supported by the MEXT/JSPS Grant-in-Aid from the Ministry of Education, Culture, Sports, Science, and Technology of Japan (JP20H05844 and JP20H05845). J.B. and J.A. are grateful for support from UC Berkeley and the UC Berkeley College of Chemistry. This research used the Savio computational cluster resource provided by the Berkeley Research Computing program at the University of California, Berkeley (supported by the UC Berkeley Chancellor, Vice Chancellor for Research, and Chief Information Officer). Y.-L.Y., Y.Z., and N.S. are grateful for support from the RIKEN pioneering project: Evolution of Matter in the Universe. This paper makes use of the following ALMA data: ADS/JAO.ALMA#2016.1.01501.S, ADS/JAO.ALMA#2017.1.01462.S., and ADS/JAO.ALMA#2022.1.00303.S. ALMA is a partnership of the ESO (representing its member states), the NSF (USA) and NINS (Japan), together with the NRC (Canada) and the NSC and ASIAA (Taiwan), in cooperation with the Republic of Chile. The Joint ALMA Observatory is operated by the ESO, the AUI/NRAO, and the NAOJ.

Facility: ALMA

7. APPENDIX: 12M + ACA IMAGES

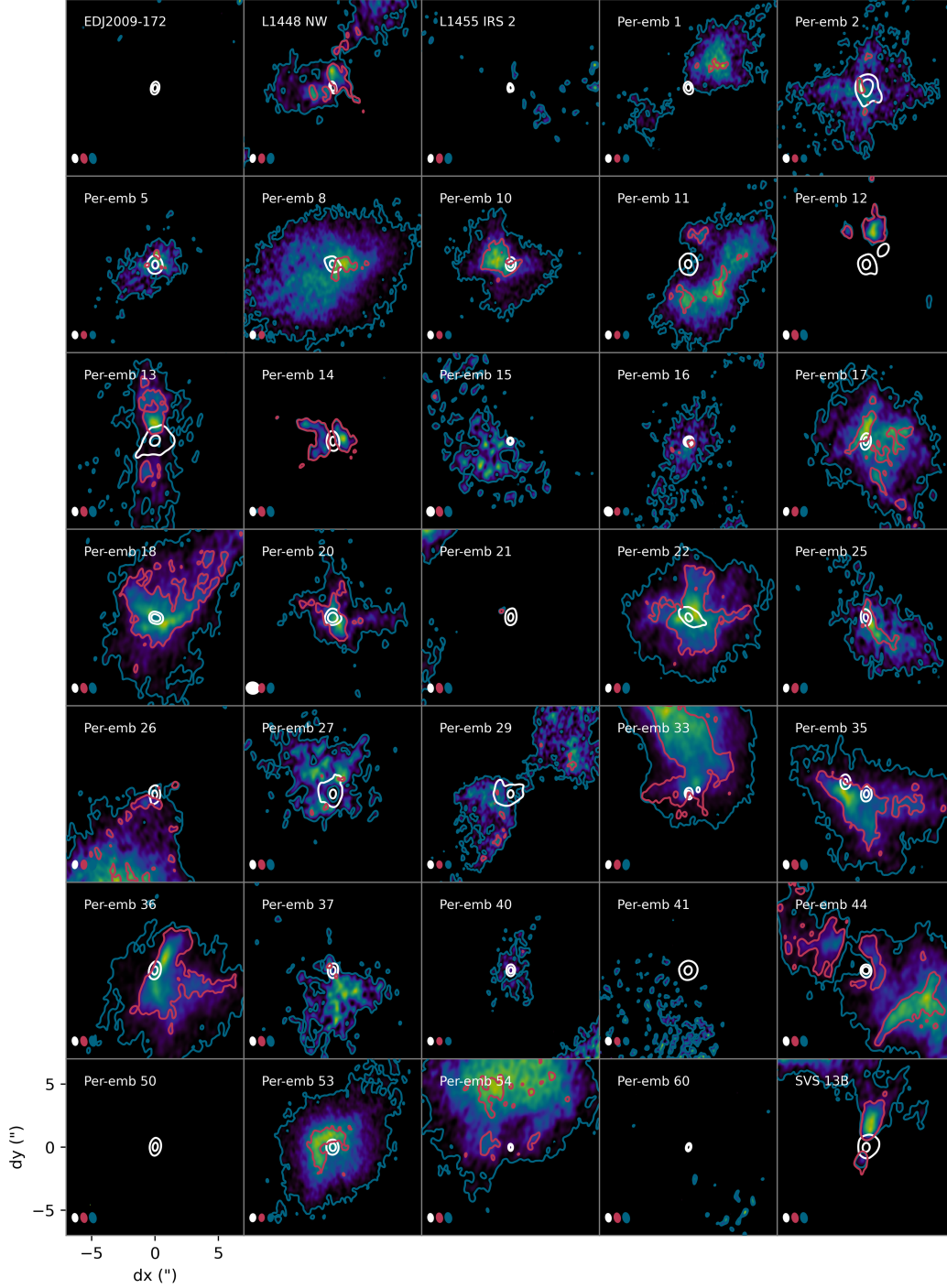


Figure 7. Combined 12m + ACA and 12m C_2H moment-0 maps. 12m moment-0 maps are contoured in red, and the combined 12m + ACA moment-0 maps are contoured in blue and shown as colormaps. The colormap minimum, and all contours are drawn at 35 mJy/beam for all sources.

In Figure 7, we present the moment-0 maps of the C_2H emission from both the 12m ALMA PEACHES data as well as the combined 12m + ACA images. The red contours show the 12m only and the blue contours and colormap show the 12m + ACA images. For all sources, the contours are drawn at 35 mJy/beam as well as the colormap minimum.

The combined 12m + ACA images, as compared to the imaging the 12m data alone contoured at the same flux of 35 mJy/beam reveals more large scale structure in the C₂H surrounding the sources, with the exception of Per-emb 14. As expected, these images still retain the general spatial morphology seen in the 12m images. As the combined 12m + ACA images are less sensitive to small scale structure, we use the 12m only images for the spatial analyses with SO in section 3.1.

8. APPENDIX: LINE AND CONTINUUM IMAGING TABLES

Table 1. Continuum Parameters

Source	Max (mJy/beam)	RMS (mJy/beam)	Beam (")
Per-emb 53	18.30	0.09	0.59 x 0.42
Per-emb 16	6.00	0.13	0.69 x 0.59
Per-emb 8	56.86	0.14	0.57 x 0.39
Per-emb 11 A	127.53	0.29	0.58 x 0.40
Per-emb 1	53.60	0.62	0.57 x 0.39
Per-emb 5	169.17	0.31	0.56 x 0.40
Per-emb 2	115.35	0.54	0.59 x 0.43
Per-emb 40	13.58	0.09	0.56 x 0.40
Per-emb 10	18.15	0.09	0.56 x 0.40
Per-emb 29	95.14	0.25	0.56 x 0.40
Per-emb-41 N/S	128.81	0.25	0.56 x 0.41
L1448 NW	56.25	0.71	0.59 x 0.36
Per-emb 33 A	155.65	0.39	0.59 x 0.36
Per-emb 26	145.36	0.48	0.60 x 0.37
Per-emb 22 A	30.46	0.17	0.59 x 0.36
Per-emb 25	86.84	0.22	0.59 x 0.37
Per-emb 17	34.07	0.17	0.59 x 0.37
Per-emb 20	8.25	0.38	1.01 x 0.93
L1455 IRS 2	2.04	0.15	0.58 x 0.37
Per-emb 44	148.83	2.13	0.63 x 0.40
Per-emb 12	502.33	1.06	0.63 x 0.40
Per-emb 13	311.00	0.51	0.63 x 0.40
Per-emb 27	141.23	0.34	0.63 x 0.40
Per-emb 54	1.62	0.09	0.63 x 0.40
Per-emb 21	43.37	0.16	0.63 x 0.40
Per-emb 14	62.19	0.14	0.63 x 0.40
Per-emb 35 A/B	21.47	0.11	0.63 x 0.40
SVS 13B	140.67	0.36	0.63 x 0.40
Per-emb 15	5.32	0.15	0.70 x 0.56
Per-emb 50	82.65	0.19	0.63 x 0.40
Per-emb 18	65.08	0.71	0.63 x 0.40
Per-emb 37	11.06	0.09	0.63 x 0.40
Per-emb 60	1.76	0.09	0.63 x 0.40
EDJ2009-172	12.94	0.09	0.63 x 0.40
Per-emb 36	112.16	0.24	0.63 x 0.40

Table 2. Line Parameters

Source	C ₂ H				SO			
	Moment 0		Channel		Moment 0		Channel	
	Max (mJy/beam*km/s)	RMS (mJy/beam*km/s)	RMS (mJy/beam)	Beam (")	Max (mJy/beam*km/s)	RMS (mJy/beam*km/s)	RMS (mJy/beam)	Beam (")
Per-emb 53	91.45	6.42	4.87	0.56 x 0.37	776.73	6.44	5.38	0.57 x 0.38
Per-emb 16	56.44	5.69	4.73	0.55 x 0.37	81.05	10.07	4.79	0.67 x 0.40
Per-emb 8	86.34	7.47	4.80	0.55 x 0.37	142.25	8.50	4.67	0.58 x 0.39
Per-emb 11 A	59.55	6.28	4.88	0.55 x 0.37	245.98	10.03	5.31	0.58 x 0.39
Per-emb 1	51.10	5.86	4.66	0.55 x 0.38	288.86	24.42	10.25	0.58 x 0.39
Per-emb 5	50.28	5.85	4.76	0.53 x 0.38	33.77	5.71	4.75	0.54 x 0.38
Per-emb 2	52.62	7.44	4.68	0.54 x 0.38	179.54	6.48	4.64	0.54 x 0.38
Per-emb 40	36.88	7.61	4.84	0.54 x 0.38	379.63	21.95	4.65	0.54 x 0.38
Per-emb 10	83.97	7.33	4.78	0.54 x 0.38	360.86	7.10	4.74	0.54 x 0.38
Per-emb 29	45.50	7.11	4.79	0.54 x 0.38	435.62	13.24	5.80	0.54 x 0.38
Per-emb 41 N/S	32.11	6.37	4.72	0.54 x 0.38	103.74	6.11	4.74	0.54 x 0.38
L1448 NW	88.36	7.01	5.32	0.68 x 0.43	411.02	7.67	5.26	0.67 x 0.43
Per-emb 33 A	197.92	8.57	5.35	0.68 x 0.43	168.93	9.04	5.48	0.67 x 0.43
Per-emb 26	66.70	5.66	5.08	0.67 x 0.43	339.26	23.78	6.23	0.67 x 0.43
Per-emb 22 A	150.10	7.25	5.12	0.68 x 0.43	601.36	12.42	5.04	0.67 x 0.43
Per-emb 25	63.27	7.85	5.13	0.70 x 0.45	538.26	6.54	5.02	0.67 x 0.43
Per-emb 17	75.88	7.86	5.21	0.68 x 0.43	2656.63	59.39	6.36	0.66 x 0.43
Per-emb 20	114.13	7.29	5.20	0.68 x 0.43	465.58	7.67	5.09	0.66 x 0.43
L1455 IRS 2	30.84	7.10	5.18	0.67 x 0.43	31.28	6.84	4.99	0.66 x 0.43
Per-emb 44	147.33	13.19	5.67	0.71 x 0.45	3794.34	15.61	5.42	0.71 x 0.45
Per-emb 12	127.98	8.34	5.65	0.71 x 0.45	1184.92	51.15	8.75	0.71 x 0.45
Per-emb 13	113.12	12.51	5.69	0.71 x 0.45	473.99	24.11	5.95	0.71 x 0.45
Per-emb 27	60.35	8.66	5.78	0.71 x 0.45	3705.70	138.48	8.31	0.71 x 0.45
Per-emb 54	78.32	9.37	5.82	0.71 x 0.45	224.24	8.54	5.64	0.71 x 0.45
Per-emb 21	73.45	11.57	5.68	0.71 x 0.45	441.03	9.14	5.50	0.71 x 0.45
Per-emb 14	111.01	7.53	5.68	0.71 x 0.45	530.19	7.26	5.42	0.71 x 0.45
Per-emb 35 A/B	168.85	7.42	5.68	0.71 x 0.45	1335.69	13.84	5.43	0.71 x 0.45
SVS 13B	149.13	7.72	5.53	0.71 x 0.45	1149.74	18.95	5.56	0.71 x 0.45
Per-emb 15	35.58	7.43	5.64	0.71 x 0.45	51.32	10.21	5.51	0.71 x 0.45
Per-emb 50	35.92	7.71	5.68	0.71 x 0.45	2270.27	46.94	6.28	0.71 x 0.45
Per-emb 18	159.19	7.21	5.62	0.71 x 0.45	1280.34	15.02	5.41	0.72 x 0.45
Per-emb 37	38.87	6.94	5.64	0.72 x 0.45	194.68	9.68	5.56	0.71 x 0.45
Per-emb 60	33.61	9.13	5.81	0.72 x 0.45	51.14	9.94	5.65	0.71 x 0.45
EDJ2009-172	37.73	8.92	5.67	0.71 x 0.45	43.44	9.95	5.50	0.72 x 0.45
Per-emb 36	230.23	8.17	5.71	0.71 x 0.45	1031.61	23.11	5.28	0.71 x 0.45

Table 3. Fitted C₂H Column Densities

Source	Log N _T (cm ⁻²)	
	Median	Range
Per-emb 53	14.47	1.34
Per-emb 16	14.36	1.16
Per-emb 8	14.59	1.51
Per-emb 11	14.48	1.21
Per-emb 1	14.36	1.05
Per-emb 5	14.28	1.49
Per-emb 2	14.42	1.05
Per-emb 40	14.29	1.00
Per-emb 10	14.42	2.03
Per-emb 29	14.11	1.32
Per-emb 41	14.18	0.92
L1448 NW	14.48	2.97
Per-emb 33	14.59	1.52
Per-emb 26	14.15	1.69
Per-emb 22	14.25	1.10
Per-emb 25	14.21	1.13
Per-emb 17	14.19	1.08
Per-emb 20	14.16	1.29
L1455 IRS 2	14.05	1.29
Per-emb 44	14.19	1.11
Per-emb 12	13.99	1.35
Per-emb 13	14.04	1.39
Per-emb 27	14.14	1.23
Per-emb 54	14.31	1.42
Per-emb 21	14.64	1.86
Per-emb 14	14.08	0.84
Per-emb 35	14.23	1.05
SVS 13B	14.49	1.86
Per-emb 15	13.97	1.15
Per-emb 50	14.01	0.91
Per-emb 18	14.27	2.18
Per-emb 37	14.00	0.39
Per-emb 36	14.32	1.07

REFERENCES

- Aikawa, Y., Furuya, K., Yamamoto, S., & Sakai, N. 2020, ApJ, 897, 110, doi: [10.3847/1538-4357/ab994a](https://doi.org/10.3847/1538-4357/ab994a)
- Arce, H. G., & Sargent, A. I. 2006, ApJ, 646, 1070, doi: [10.1086/505104](https://doi.org/10.1086/505104)
- Artur de la Villarmois, E., Guzmán, V. V., Yang, Y. L., Zhang, Y., & Sakai, N. 2023, A&A, 678, A124, doi: [10.1051/0004-6361/202346728](https://doi.org/10.1051/0004-6361/202346728)
- Artur de la Villarmois, E., Jørgensen, J. K., Kristensen, L. E., et al. 2019, A&A, 626, A71, doi: [10.1051/0004-6361/201834877](https://doi.org/10.1051/0004-6361/201834877)
- Bachiller, R., & Pérez Gutiérrez, M. 1997, ApJL, 487, L93, doi: [10.1086/310877](https://doi.org/10.1086/310877)
- Bergin, E. A., Du, F., Cleeves, L. I., et al. 2016, ApJ, 831, 101, doi: [10.3847/0004-637X/831/1/101](https://doi.org/10.3847/0004-637X/831/1/101)
- Bergin, E. A., Goldsmith, P. F., Snell, R. L., & Langer, W. D. 1997, ApJ, 482, 285, doi: [10.1086/304108](https://doi.org/10.1086/304108)

- Bergner, J. B., Öberg, K. I., Bergin, E. A., et al. 2019, *ApJ*, 876, 25, doi: [10.3847/1538-4357/ab141e](https://doi.org/10.3847/1538-4357/ab141e)
- . 2020, *ApJ*, 898, 97, doi: [10.3847/1538-4357/ab9e71](https://doi.org/10.3847/1538-4357/ab9e71)
- Booth, A. S., Law, C. J., Temmink, M., Leemker, M., & Macías, E. 2023, *A&A*, 678, A146, doi: [10.1051/0004-6361/202346974](https://doi.org/10.1051/0004-6361/202346974)
- Booth, A. S., Leemker, M., van Dishoeck, E. F., et al. 2024, *AJ*, 167, 164, doi: [10.3847/1538-3881/ad2700](https://doi.org/10.3847/1538-3881/ad2700)
- Bosman, A. D., Alarcón, F., Zhang, K., & Bergin, E. A. 2021, *ApJ*, 910, 3, doi: [10.3847/1538-4357/abe127](https://doi.org/10.3847/1538-4357/abe127)
- Calahan, J. K., Bergin, E. A., Bosman, A. D., et al. 2023, *Nature Astronomy*, 7, 49, doi: [10.1038/s41550-022-01831-8](https://doi.org/10.1038/s41550-022-01831-8)
- Cortes, P., Vlahakis, C., Hales, A., et al. 2023, *ALMA Cycle 11 Technical Handbook*, doi: [10.5281/zenodo.7822943](https://doi.org/10.5281/zenodo.7822943)
- Curtis, E. I., Richer, J. S., Swift, J. J., & Williams, J. P. 2010, *MNRAS*, 408, 1516, doi: [10.1111/j.1365-2966.2010.17214.x](https://doi.org/10.1111/j.1365-2966.2010.17214.x)
- Du, F., Bergin, E. A., & Hogerheijde, M. R. 2015, *ApJL*, 807, L32, doi: [10.1088/2041-8205/807/2/L32](https://doi.org/10.1088/2041-8205/807/2/L32)
- Dunham, M. M., Arce, H. G., Mardones, D., et al. 2014a, *ApJ*, 783, 29, doi: [10.1088/0004-637X/783/1/29](https://doi.org/10.1088/0004-637X/783/1/29)
- Dunham, M. M., Evans, N. J., Bourke, T. L., et al. 2010, *ApJ*, 721, 995, doi: [10.1088/0004-637X/721/2/995](https://doi.org/10.1088/0004-637X/721/2/995)
- Dunham, M. M., Stutz, A. M., Allen, L. E., et al. 2014b, in *Protostars and Planets VI*, ed. H. Beuther, R. S. Klessen, C. P. Dullemond, & T. Henning, 195–218, doi: [10.2458/azu_uapress.9780816531240-ch009](https://doi.org/10.2458/azu_uapress.9780816531240-ch009)
- Guzmán, V. V., Bergner, J. B., Law, C. J., et al. 2021, *ApJS*, 257, 6, doi: [10.3847/1538-4365/ac1440](https://doi.org/10.3847/1538-4365/ac1440)
- Harsono, D., Bjerkeli, P., van der Wiel, M. H., et al. 2018, *Nature Astronomy*, 2, 646
- Harsono, D., Persson, M. V., Ramos, A., et al. 2020, *A&A*, 636, A26, doi: [10.1051/0004-6361/201935994](https://doi.org/10.1051/0004-6361/201935994)
- Hatchell, J., Fuller, G. A., & Richer, J. S. 2007, *A&A*, 472, 187, doi: [10.1051/0004-6361:20066467](https://doi.org/10.1051/0004-6361:20066467)
- Heays, A. N., Bosman, A. D., & van Dishoeck, E. F. 2017, *A&A*, 602, A105, doi: [10.1051/0004-6361/201628742](https://doi.org/10.1051/0004-6361/201628742)
- Hollenbach, D., Kaufman, M. J., Bergin, E. A., & Melnick, G. J. 2009, *ApJ*, 690, 1497, doi: [10.1088/0004-637X/690/2/1497](https://doi.org/10.1088/0004-637X/690/2/1497)
- Imai, M., Oya, Y., Svoboda, B., et al. 2022, *ApJ*, 934, 70, doi: [10.3847/1538-4357/ac77e7](https://doi.org/10.3847/1538-4357/ac77e7)
- Jansen, D. J., Spaans, M., Hogerheijde, M. R., & van Dishoeck, E. F. 1995, *A&A*, 303, 541
- Jiménez-Serra, I., Martín-Pintado, J., Rodríguez-Franco, A., & Martín, S. 2005, *ApJL*, 627, L121, doi: [10.1086/432467](https://doi.org/10.1086/432467)
- Krijt, S., Bosman, A. D., Zhang, K., et al. 2020, *ApJ*, 899, 134, doi: [10.3847/1538-4357/aba75d](https://doi.org/10.3847/1538-4357/aba75d)
- Krijt, S., Schwarz, K. R., Bergin, E. A., & Ciesla, F. J. 2018, *ApJ*, 864, 78, doi: [10.3847/1538-4357/aad69b](https://doi.org/10.3847/1538-4357/aad69b)
- Lada, C. J. 1987, in *Symposium-International astronomical union*, Vol. 115, Cambridge University Press, 1–18
- Manara, C. F., Morbidelli, A., & Guillot, T. 2018, *A&A*, 618, L3, doi: [10.1051/0004-6361/201834076](https://doi.org/10.1051/0004-6361/201834076)
- Maury, A. J., André, P., Testi, L., et al. 2019, *A&A*, 621, A76, doi: [10.1051/0004-6361/201833537](https://doi.org/10.1051/0004-6361/201833537)
- McMullin, J. P., Waters, B., Schiebel, D., Young, W., & Golap, K. 2007, in *Astronomical Society of the Pacific Conference Series*, Vol. 376, *Astronomical Data Analysis Software and Systems XVI*, ed. R. A. Shaw, F. Hill, & D. J. Bell, 127
- Miotello, A., Facchini, S., van Dishoeck, E. F., et al. 2019, *A&A*, 631, A69, doi: [10.1051/0004-6361/201935441](https://doi.org/10.1051/0004-6361/201935441)
- Myers, P. C., Adams, F. C., Chen, H., & Schaff, E. 1998, *ApJ*, 492, 703, doi: [10.1086/305048](https://doi.org/10.1086/305048)
- Myers, P. C., & Ladd, E. F. 1993, *ApJL*, 413, L47, doi: [10.1086/186956](https://doi.org/10.1086/186956)
- Nagy, Z., Ossenkopf, V., Van der Tak, F. F. S., et al. 2015, *A&A*, 578, A124, doi: [10.1051/0004-6361/201424220](https://doi.org/10.1051/0004-6361/201424220)
- Okoda, Y., Oya, Y., Sakai, N., et al. 2018, *ApJL*, 864, L25, doi: [10.3847/2041-8213/aad8ba](https://doi.org/10.3847/2041-8213/aad8ba)
- Oya, Y., Sakai, N., Watanabe, Y., et al. 2018, *ApJ*, 863, 72, doi: [10.3847/1538-4357/aacf42](https://doi.org/10.3847/1538-4357/aacf42)
- Oya, Y., Sakai, N., Sakai, T., et al. 2014, *ApJ*, 795, 152, doi: [10.1088/0004-637X/795/2/152](https://doi.org/10.1088/0004-637X/795/2/152)
- Parker, N. D., Padman, R., & Scott, P. F. 1991, *MNRAS*, 252, 442, doi: [10.1093/mnras/252.3.442](https://doi.org/10.1093/mnras/252.3.442)
- Sakai, N., Saruwatari, O., Sakai, T., Takano, S., & Yamamoto, S. 2010, *A&A*, 512, A31, doi: [10.1051/0004-6361/200913098](https://doi.org/10.1051/0004-6361/200913098)
- Sakai, N., & Yamamoto, S. 2013, *Chemical Reviews*, 113, 8981, doi: [10.1021/cr4001308](https://doi.org/10.1021/cr4001308)
- Sakai, N., Oya, Y., Sakai, T., et al. 2014a, *ApJL*, 791, L38, doi: [10.1088/2041-8205/791/2/L38](https://doi.org/10.1088/2041-8205/791/2/L38)
- Sakai, N., Sakai, T., Hirota, T., et al. 2014b, *Nature*, 507, 78, doi: [10.1038/nature13000](https://doi.org/10.1038/nature13000)
- Sakai, N., Oya, Y., Higuchi, A. E., et al. 2017, *MNRAS*, 467, L76, doi: [10.1093/mnras/176/4/L76](https://doi.org/10.1093/mnras/176/4/L76)
- Stephens, I. 2019, *Top Level README - MASSES Full Data Release, V1*, Harvard Dataverse, doi: [10.7910/DVN/N5ISPG](https://doi.org/10.7910/DVN/N5ISPG)
- Stephens, I. W., Bourke, T. L., Dunham, M. M., et al. 2019, *ApJS*, 245, 21, doi: [10.3847/1538-4365/ab5181](https://doi.org/10.3847/1538-4365/ab5181)
- Tobin, J. J., Looney, L. W., Li, Z.-Y., et al. 2016, *ApJ*, 818, 73, doi: [10.3847/0004-637X/818/1/73](https://doi.org/10.3847/0004-637X/818/1/73)
- Tobin, J. J., Sheehan, P. D., Megeath, S. T., et al. 2020, *The Astrophysical Journal*, 890, 130

- Tychoniec, L., van Dishoeck, E. F., van't Hoff, M. L. R.,
et al. 2021, A&A, 655, A65,
doi: [10.1051/0004-6361/202140692](https://doi.org/10.1051/0004-6361/202140692)
- Van Clepper, E., Bergner, J. B., Bosman, A. D., Bergin, E.,
& Ciesla, F. J. 2022, ApJ, 927, 206,
doi: [10.3847/1538-4357/ac511b](https://doi.org/10.3847/1538-4357/ac511b)
- Yang, Y.-L., Sakai, N., Zhang, Y., et al. 2021, ApJ, 910, 20,
doi: [10.3847/1538-4357/abdfd6](https://doi.org/10.3847/1538-4357/abdfd6)
- Zhang, K., Schwarz, K. R., & Bergin, E. A. 2020, ApJL,
891, L17, doi: [10.3847/2041-8213/ab7823](https://doi.org/10.3847/2041-8213/ab7823)
- Zhang, Y., Higuchi, A. E., Sakai, N., et al. 2018, ApJ, 864,
76, doi: [10.3847/1538-4357/aad7ba](https://doi.org/10.3847/1538-4357/aad7ba)
- Zhang, Z. E., Yang, Y.-l., Zhang, Y., et al. 2023, ApJ, 946,
113, doi: [10.3847/1538-4357/acbdf7](https://doi.org/10.3847/1538-4357/acbdf7)